International Journal of High-Rise Buildings
www.ctbuh-korea.org/ijhrb/index.php

International Journal of High-Rise Buildings
December 2022, Vol 11, No 4, 287-300
https://doi.org/10.21022/IJHRB.2022.11.4.287

Experimental and Computational Investigation of Wind Flow Field on a Span Roof Structure

K B Rajasekarababu[1], G Vinayagamurthy[2†], and Ajay Kumar T M[3] , Selvirajan S[4]

[1]*AIWE-LAB, School of Civil and Environmental Engineering, Harbin Institute of Technology,Shenzhen 518055, China*
[2]*Aerodynamics laboratory, Centre for Innovation and Product Development, Vellore Institute ofTechnology Chennai, India*
[3]*Assistant Manager, Design & Engineering, L&T Energy Hydrocarbon, India*
[4]*Wind Engineering Lab, CSIR- Structural Engineering Research Center, India*

Abstract Unconventional structures are getting more popular in recent days. Large-span roofs are used for many structures, such as airports, stadiums, and conventional halls. Identifying the pressure distribution and wind load acting on those structures is essential. This paper offers a collaborative study of computational fluid dynamics (CFD) simulations and wind tunnel tests for assessing wind pressure distribution for a building with a combined slender curved roof. The hybrid turbulence model, Improved Delayed Detached Eddy Simulation (IDDES), simulates the open terrain turbulent flow field. The wind-induced local pressure coefficients on complex roof structures and the turbulent flow field around the structure were thus calculated based upon open terrain wind flow simulated with the FLUENT software. Local pressure measurements were investigated in a boundary layer wind tunnel simultaneous to the simulation to determine the pressure coefficient distributions. The results predicted by CFD were found to be consistent with the wind tunnel test results. The comparative study validated that the recommended IDDES model and the vortex method associated with CFD simulation are suitable tools for structural engineers to evaluate wind effects on long-span complex roofs and plan irregular buildings during the design stage.

Keywords Large span roofs, Local pressure coefficient, Wind pressure coefficients, IDDES CFD, Terrain wind flow

†Corresponding author:
G Vinayagamurthy
Tel: +
E-mail:
vinayagamurthy.g@vit.ac.in

1. Introduction

Large roofs provide architects and designers with substitutes for regular rectangular building types. They are generally utilized in large-scale buildings like leisure centres, exhibition centres, airports, and shopping malls, as it can provide ample space without inner columns C.L.Lu. et al. (2012). These rooftop structures comprise lightweight materials (glass boards) and often less natural frequencies and damping ratios, susceptible to wind forces. Hence, wind loads seek attention while designing such structures. However, the recent wind codes and standards have not entirely covered the wind-resistant design of such long-span curved roof structures and unique structures by Guide, Residential Structural Design from Coulbourne Consulting (2017).

This investigation emphasizes the determination of pressure distribution on a long-span roof structure (Chennai international airport structure), one of India's busiest airports (shown in Figure. 1), handling over 22.5 million passengers annually. The distribution of pressure and wind flow on the building is affected due to a broad range of parameters

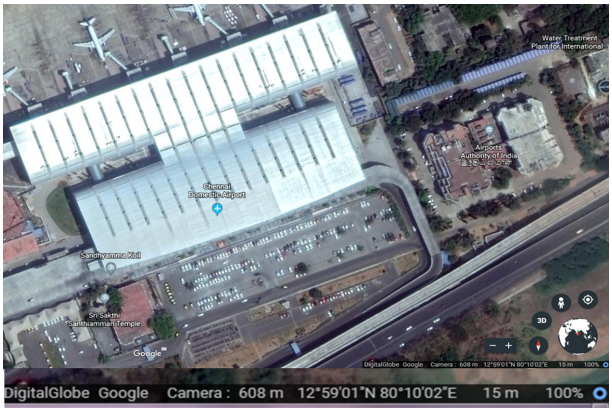


Figure. 1. Long roof Chennai airport terminal building. (satellite view)

such as approach-flow conditions, building geometry, topographic surroundings, and wind directions Montazeri et al. (2013). Consequently, it requires extensive research and creative computational and test approaches to determine the local pressure coefficient on sensitive curved roof structures. Moreover, the wind-induced loads and flow on/ around the building and its components (facades) are estimated by understanding their local pressure distributions. Above all, the local surface pressure distributions on the roofs and walls affect buildings with long-span roofs.

Wind tunnel test is comparatively an established practising method in wind engineering studies. Full-scale measurements can be employed to obtain more reliable data on airflow and pressure distribution in the building. On the other hand, wind tunnel tests on small-scale models are usually favoured as they permit the control of wind speed and heading as well as the study of different configurations. Wind tunnel testing is the most prominent and most effective tool for estimating wind load on unique structures. Kernot was the first to conduct a wind tunnel on a tall building. Another widely practised technique is computational fluid dynamics (CFD), which utilizes the numerical solution for the set of governing flow field equations. CFD practice is extensively used to calculate wind flows around bluff bodies such as buildings and structures. Because of the advancements in computational mechanics, collective utilization of CFD is seen in building practices. Three computational methods generally adopted in Computational Wind Engineering, viz. Reynolds averaged Navier–Stokes (RANS) modelling, Large Eddy Simulation (LES) and Hybrid models (RANS + LES). RANS modelling resolves time-averaged flow parameters by using turbulence modelling, which requires a less computational resource, but has significant drawbacks such as it cannot appropriately calculate the airflow around buildings and computes only the mean flow parameters and wind loads. However, LES divides eddies into large and small sizes in which the large eddies are modelled in three-dimensional and time-dependent manner while modelling the little eddies with a subgrid-scale model, which results in high computational time and resources.

Hybrid model bridges the RANS and LES branches amalgamating the SGS (Sub-Grid Scale) and RANS eddy viscosities. In hybrid (RANS/LES) simulations, RANS equations help in solving the near-wall region of the building, and the filtered outer layer is solved for the boundary layer by LES. The blending function involved is dependent on the length scale ratios of the outer and inner regions, as discussed by Gieseking et al. (2013). The hybrid LES/ RANS, DES has been widely used to deal with high Reynolds number separated flows, as suggested by Spalart et al. (2006). RANS is used in attached boundary layers in DES to characterize a length scale that determines the model used at a grid point.

DDES and IDDES proposed by Spalart et al. (1997) and Shur et al. (2008), respectively, are refreshed forms of the DES model capable of compensating the tribulations of grid-induced separation (GIS) and log-layer mismatch (LLM). In contrast, the LES model is utilized in the outer layer and separation regions. These hybrid methodologies have also been employed in academic research, and engineering applications by Balakrishnan et al. (2010), Gritskevich et al. (2012), Guseva et al. (2016), Xiao et al. (2015 a,b), & Liu et al. (2016 and 2019), comparing the performance of RANS, LES and DES turbulence models approaches on simulating airflow around the buildings. The results seem to be similar to LES. Thus, DDES reproduces the wind flow field similar to LES with less mesh and computation time. IDDES turbulence models provide more precise predictions than URANS models, especially in the wake region, including the mean streamwise velocity profile and mean pressure coefficient on the surface by Ke et al. (2019). The use of hybrid models (DDES and IDDES) in building aerodynamics to determine the wind pressure coefficients on a setback back verified the same with experiments, which seem to have a good agreement among the results Rajasekarababu et al. (2019 a,b and 2020). Moreover, notably, IDDES shows significant potential in environmental wind simulations.

Due to the large dimension of the building and high wind speed, the building's wind is commonly a typical bluff-body turbulent flow (with a high Reynolds number). Therefore, CFD techniques should propose a faithful model of wind turbulence within the atmospheric boundary layer at high Reynolds numbers. Therefore, it is anticipated that the recommendation of CFD simulations and another associated hybrid turbulence model (IDDES) can provide an efficient result for architects, builders, and urban planners to evaluate the wind effects on large-span curved roofs. The primary focus of this study is to find a practical method for estimating wind effects on a large-span curved-roof structure using the IDDES turbulence model. The IDDES approach has been used in this paper to find the local wind pressure coefficients on the unique large roof structure, which comprises two curved roof structures with different directions, as shown in Figure. 2. (Atmospheric Boundary

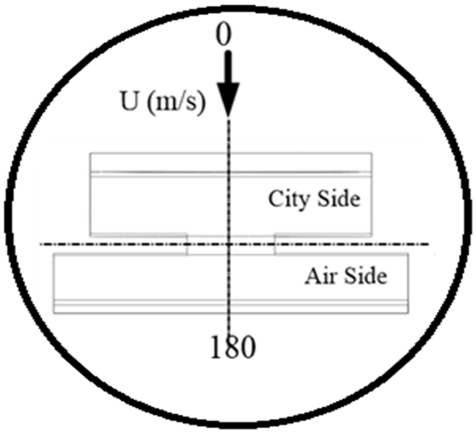


Figure. 2. A typical view long roof structure with different wind directions.

Layer) ABL wind tunnel pressure data and local pressure coefficients are obtained and compared with computational results. Furthermore, the precision and reliability of the computational frame are also discussed.

2. Methodology

2.1. Wind tunnel testing

A wind tunnel test for the roof structure was carried out at the boundary layer wind tunnel in the Wind Engineering Laboratory of SERC- CSIR Chennai. The open-circuit wind tunnel configuration with test section dimension, L × B × H = 2.5 × 2.1 × 18 m, is utilized. The model of the whole structure terminal was made with a 1:300 geometric scale, and the dimensions are shown in Figure. 3(a). The wind tunnel model consists of 285 pressure taps and is distributed through the model along with the locations of interest, such as curved sections on the windward and leeward surfaces and connector building. The pressure tap layouts on the cityside, airside and connector building are shown in Figure. 3 (b). The pressure data were acquired using PSI pressure scanners for a sampling period of 23 seconds at a sampling rate of 650 Hz. The time-series data of Cp was analyzed using MATLAB. As the airport terminal surrounds a few small buildings and hills, the airport terrain is considered open terrain (category B) as specified in IS 875- part 3 (2015). Figure. 3 (b) shows the roughness elements in front of the test section.

2.2. Numerical simulation

Many aspects have been considered, such as the computational domain, inflow boundary conditions, mesh

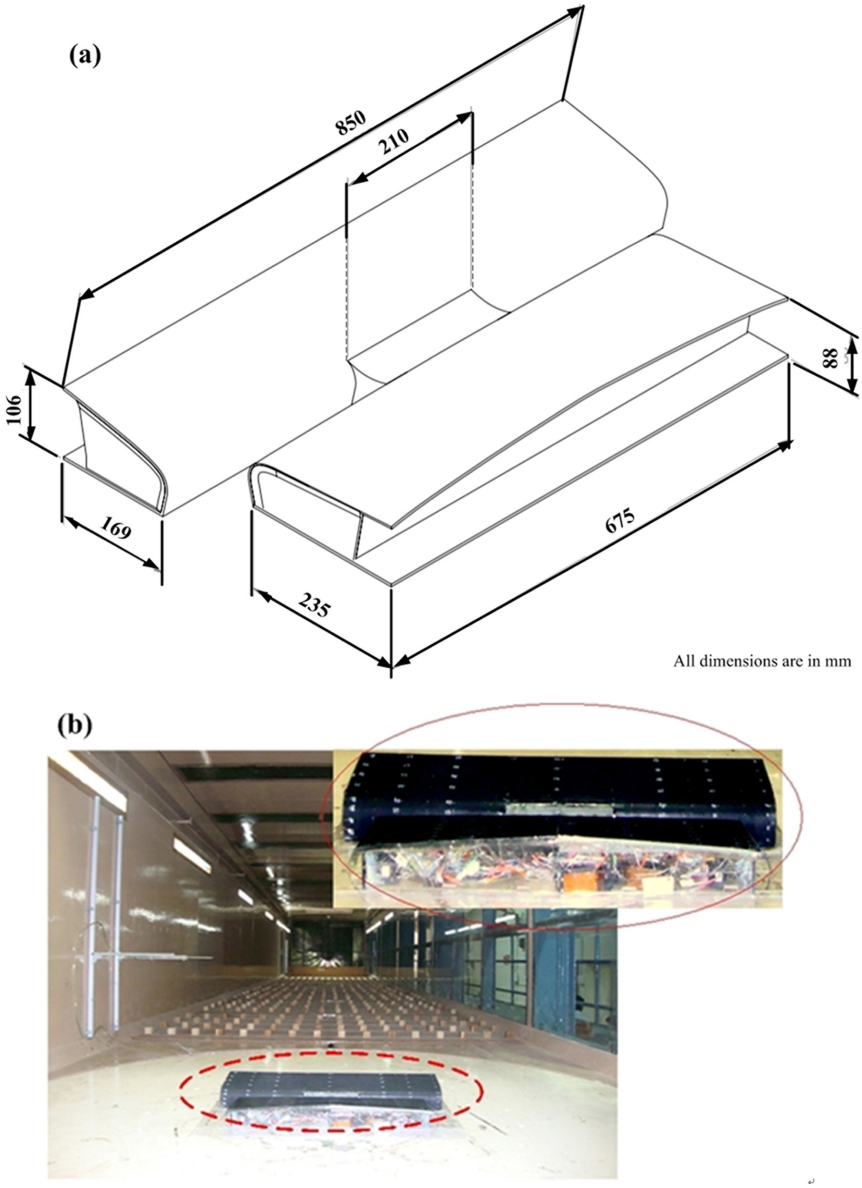


Figure. 3. (a) Dimensions of the scaled model (b) Scaled model inside the wind tunnel test section.

generation, solver settings, and residual control in picking a suitable turbulence model and accomplishing precise computational outcomes. To guarantee that the reliability of the simulation is kept up to higher precision, better consideration has been taken in deciding and using the solver settings and inlet boundary conditions.

2.3. Computational case description

Under the uniform, open atmospheric boundary layer, the wind tunnel test section measurements and inlet wind flows were performed. The computational domain dimensions are X × Y × Z = 3 m × 1.8 m × 7 m, as shown in Figure. 4. The roof structure terminal dimension is L × B × H = 0.7 m × 0.38 m × 0.095 m for $\alpha = 0^0$. The maximum blockage ratio was found to be 0.6 % in this investigation, which is less than the 3% recommended limit by Blocken et al. (2014) and Franke et al. (2007 and 2011). In general, the computational complexity and accuracy of the results are defined by the magnitude and quality of the grid. The majority of the grid element quality values are between 0.4 and 1.0, where more than 60% of the grids fall on 0.55. Thus, all the tetrahedral grids satisfy the requirements of computational simulations (Grid shown in Figure. 4). The first wall distance for open terrain is 0.0020 m, followed by Blocken et al. (2007) and Montazeri et al. (2013), and all grids have a stretching ratio of 1.12, and the grid comprises with eight prism layers being generated around the roof structure, which can be seen in Fig. 4. The grids were done in ICEM CFD (ANSYS 18.0). Grid independence study is significant in reducing errors and computational hours. Hence three grids, namely: fine (m3), medium (m2), and course (m1), as shown in Figure. 5 (a), were made by increasing the number of elements. Grid details are shown in Table 1. Results of the grid independence test in terms of mean pressure coefficient (Cp) at the mid-section of the airport faces are shown in Figure. 5(b). The result directs that fine (m3) grids are good at providing results close to the experimental result. As a result, a fine (m3) grid is retained for this investigation.

Table.1. Grid resolution size and elements

Grid resolution	Δx (m)	No. Elements
Coarse (Grid A) m1	0.0085	3775924
Medium (Grid B) m2	0.0040	7689172
Fine (Grid C) m3	0.0020	10748325

2.4. Turbulence model

The hybrid turbulence model (RANS/LES) method, a background of the RANS turbulence model (SST model) by Menter, Florian R (1994) is used in this computational simulation. Becoming fully aware that the length scale $\tilde{l}$, destruction term $D_k = \rho k^{3/2}/\tilde{l}$ substitution in the k- transport equation is to reform the basic SST model. The basic SST turbulence model $\tilde{l} = l_{RANS} = k^{1/2}$, RANS, replaces the length scale with LES ($l_{LES} = C_{SGS\Delta}$), and this reformed SST model can be utilized as a subgrid-scale model. Using blending functions, the hybrid method of turbulence model can be fabricated through different length scales Strelets, M (2001).

$$\tilde{l} = f_{blend} l_{RANS} + (1 - f_{blend}) l_{LES} \quad (1)$$

In this article, the IDDES turbulence model is used, and the grid length scale Δ is set to $\Delta = \min\{\max[C_w d_w, Cwh_{max}, h_{wn}], h_{max}\}$ followed by Shur et al. (2008).

2.4.1. Improved Delayed Detached Eddy Simulation (IDDES)

IDDES model allows simulating WMLES (Walls Modelling LES) mode in unsteady inlet conditions. The LES can simulate wall boundary layers at a higher Reynolds number than the standard LES turbulence model. The combination of the efficiency of RANS and the accuracy of LES in this turbulence model makes this approach applicable to various wind engineering applications.

When IDDES uses WALES's length scale,

$$l_{IDDES} = l_{WALES} = f_{blend}(1 + f_e) l_{RANS} + (1 - f_{blend}) l_{LES} \quad (2)$$

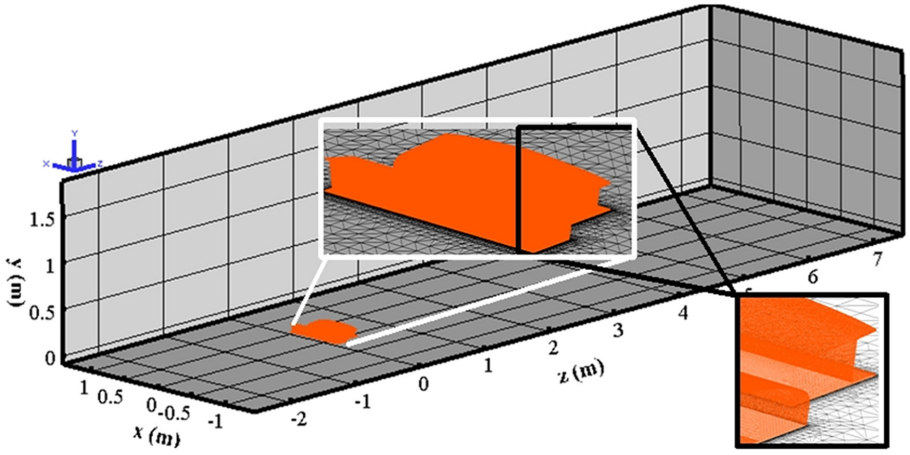


Figure 4. Perspective view of the computational domain and mesh.

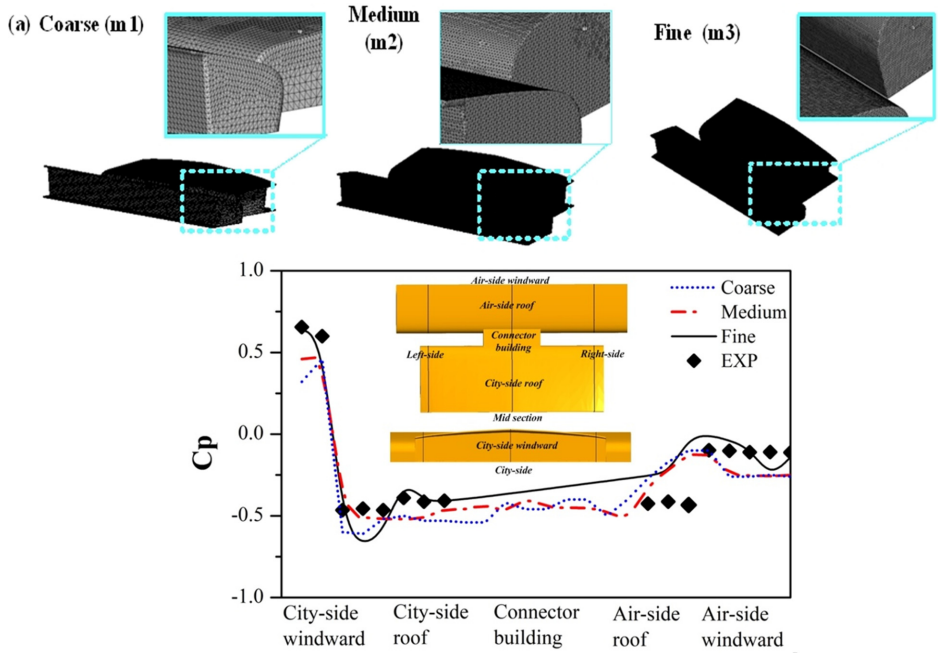


Figure 5. (a) Perspective view of three grids (b) Comparison of pressure coefficients for the three grids. (midsection)

In equation (1), elevating function (f_e) prevents the eddy viscosity in the RANS region near the transition region.

$$f_{blend} = min(2\exp(-9\alpha^2), 1.0) \tag{3}$$

$$f_e = max\{(f_{e1} - 1, 0)\}\psi f_{e2} \tag{4}$$

Here $\alpha = 0.25 - d_w/h_{max}$, where d_w is wall distance and max grid length scale.

$$f_{e1} = \begin{cases} 2\ exp(-11.09\alpha^2) & \text{if } \alpha \geq 0 \\ 2\ exp(-9.0\alpha^2) & \text{if } \alpha > 0 \end{cases} \tag{5}$$

$$f_{e2} = 1.0 - \max(f_t, f_1) \tag{6}$$

$$f_t = tanh[(c_t^2 r_{dt})^3],\ f_1 = tanh[(c_l^2 r_{dt})^{10}] \tag{7}$$

$$r_{dt} = \frac{\nu_t}{\max\{\sqrt{U_{ij}U_{ij}}, 10^{10}\}k^2 d^2} \tag{8}$$

$$r_l = \frac{\nu}{\max\{\sqrt{U_{ij}U_{ij}}, 10^{10}\}k^2 d^2} \tag{9}$$

Where c_t,c_l is the empirical constants and ψ indicates the empirical function set to 1, followed by Shur et al. (2008). The blending function (f_{blend}) takes action on the transition from RANS to LES.

2.5. Boundary conditions and solution methods

An open area surrounds the airport structure with some hills and small buildings. Thus, the topography is regarded as a transition open terrain in this investigation. The open terrain wind flow is modelled using a user-defined function in ANSYS FLUENT 18.0 (2020). This section presents the boundary conditions of the atmospheric boundary layer, including turbulence modelling and solver settings.

2.5.1. Features of ABL

The significant characteristics of the neutral Atmospheric Boundary Layer consist of the length scale distribution, turbulent intensity distribution, roughness length, Reynolds shear stress, and mean velocity profile. The environmental

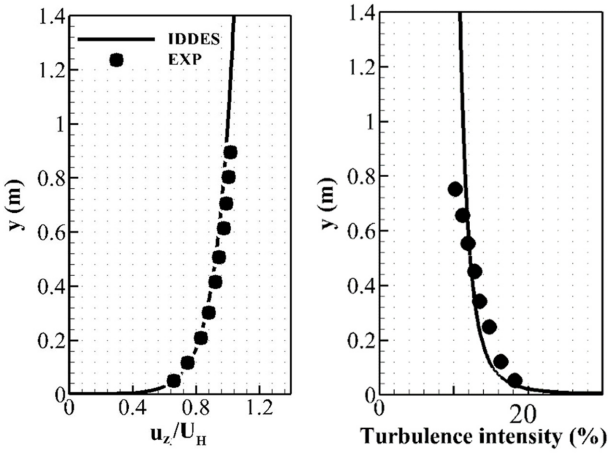


Figure 6. Open terrain inlet profile. (Velocity and Turbulence intensity)

research groups and wind engineering experts have approached the logarithmic law equation (10) to define the ABL profile's mean velocity. In this simulation, the generation of ABL is imposed based on wind tunnel flow characteristic magnitudes. The wind profiles are shown in Fig. 6.

$$(U_y) = \frac{u^*_{ABL}}{\kappa} \ln\left(\frac{y+y_o}{y_o}\right) \tag{10}$$

Where y_o denotes the roughness length, and u*ABL denotes the ABL friction velocity, determined based on the AIJ guidelines 2008 (Architectural Institute of Japan) by Tominaga et al. (2008). Here, κ indicates the Karman constant (0.42), y is the maximum height coordinate, and Cμ is the empirical constant (0.09). The turbulent intensity (I) is a significant factor governing the wind separation flow characteristics and is calculated using equation (11).

$$I(y) = \frac{1}{\ln\left(\frac{y}{y_o}\right)} \tag{11}$$

This simulation has adopted the IDDES turbulence model in the formulation of k-ω SST. Thus using the below equations (12) and (13), the factors including the turbulence dissipation rate (ε(y)) and the specific rate of dissipation (ω(y)), is taken into consideration.

$$\varepsilon(y) = \frac{u^{*3}}{\kappa(y+y_0)} \tag{12}$$

$$\omega(y) = \frac{\varepsilon(y)}{C\mu k(y)} \tag{13}$$

Therefore, turbulent kinetic energy (k(y)) could be predicted using equation (14), where a indicates a constant depending on turbulent fluctuations following Ramponi et al. (2012). Here, the value of a has been chosen as recommended by Tominaga et al. (2008).; a value can be set from 0.5 to 1.5.

$$k(y) = a(I(y)(U_y)) \tag{14}$$

ANSYS FLUENT is not specially designed for wind engineering problems. The sand grain elements create shear-like roughness and are modified to create roughness elements. Using equation (15), the open terrain boundary layers are generated to modify the roughness height. The inlet wind velocity profiles are defined according to the log-law with y_o = 1.95 mm from equation (10). The turbulence dissipation rate (ε (y)), the Specific rate of dissipation (ω(y)) and turbulent kinetic energy (k(y)) is determined according to the above equations (10-14). ABL simulations were done by modifying the roughness length for different terrains, where Ks = 0.00195 m for open terrain. Equation [15] is used to derive the relationship between aerodynamic roughness length y_0 and ground roughness.

$$K_s = \frac{9.793 y_0}{C_s} \tag{15}$$

The values of the roughness parameters, i.e. the sand-grain roughness height Ks (m) and the constant roughness C_S, were determined using their consistency relationship with the aerodynamic roughness length y_o derived by Tominaga et al. (2008). and Blocken et al. (2007). The stationary wall function is chosen on the building faces with roughness constant, C_S = 0.5 and roughness length, Ks = 0. The height of sand grain roughness is modelled using equation (15) for open terrain. The outlet of the domain is applied with zero static pressure, and the sidewalls and top of the domain are used with wall-type and symmetry boundary conditions, respectively. Fig. 6. shows minor discrepancies in the inlet velocity and turbulence intensity profiles in the streamwise gradients for open terrain, which is a significant quality measure for the computational simulation.

2.6. Solver Settings and control

This simulation is performed on ANSYS FLUENT 18.0, where the algorithm for pressure-velocity coupling applied is the SIMPLE (Semi-Implicit Method for Pressure-Linked Equations). 3-D unsteady URANS equation was solved in IDDES with the combination of Shear Stress Transport. The Least Square Cell-Based method was used as the gradient for spatial discretization in the pressure-based solver. The second-order upwind scheme was chosen for pressure, momentum, turbulent kinetic energy, and turbulent dissipation rate. The convergence is assumed to be achieved when all the scaled residuals are levelled off, and the XYZ momentum, K, ω and continuity are set to at least 10^{-5}. The assumed residuals of the computational simulation were accomplished and observed over a considerable period.

3. Result and Discussion

3.1. Validation of computational results with wind tunnel experiment

The pressure coefficient at the location on the model's surface is defined sing equation (16).

$$C_{pi}(t) = \frac{p_i(t)}{0.5\rho V^2_{ref}} \tag{16}$$

Where p_i *(t)* is the surface pressure calculated at location *i*; V_{ref} is the reference wind speed at the reference height (10.5 m/s), and ρ indicates air density.

The root mean square pressure coefficients (Cp_{rms}) obtained by the fluctuating pressure coefficient is given in below equation (17)

$$\tilde{p} = \left[\frac{1}{T}\int [p(t)-p]^2 dt\right]^{1/2} \tag{17}$$

$$\bar{p} = \frac{1}{T}\int_0^T p(t)dt$$

$\tilde{p}$ is the r.m.s pressure to the reference dynamic velocity, $\bar{p}$ is the mean pressure obtained for a time 'T'.

3.1.1. Mean pressure coefficients (Cp)

The contour and graph depict the mean wind pressure coefficients on the main roof structure obtained from the IDDES and experiment for 0^0, 40^0, 50^0, 90^0, and 180^0. In Figure. 7, pressure traces are outlined in the mentioned line for comparison purposes for the experiment and CFD. To briefly understand the local pressure distribution on the roof structure, the sections are discretized into three; Left-Section (L.S.), Mid-section (M.S.), and Right-section (R.S.), which is plotted against the local pressure coefficients for different wind incidence angle 0^o - 180^o with an interval of 10^o. The results reveal that the wind incidence angles 0^o, 40^o, 50^o, 90^o, and 180^o seem to be more critical than other angles, and thus the flow in the most critical angles is explained in detail.

For 0^o AOI (Angle of Incidence), the wind approaches the city-side windward region and experiences severe stagnation. The flow gets sheared at the separation point and accelerates over the city-side roof. The flow further moves towards the airside roof for the mid-section, whereas the left and right sections experience a suction pressure on the gable ends (end of the roof) of the city and airside building. From Figure. 8(a) and 9(a), it can be seen that there is a strong suction at the gable ends of the city and airside building with a minimum local pressure coefficient of about –0.8 on both the sections and a local pressure coefficient of 0.8 at the windward of the city-side due to stagnation.

High suctions are induced for 40° and 50° wind angle incidences where the minimum local pressure coefficient of –1.5 is observed in the edge near the city side roof corner. It is evident that there is a shear at the leading edge of the city side roof and reattaches on the airside roof, and thus a part of the airside roof experiences a pressure gradient towards the downstream. A reasonably high-pressure gradient is observed in the area (see Figure. 8(b) & 8(c)) due to the large suction developed when the direction of heading wind at 40^o and 50^o compared to those under 0^o, 90^o and 180^o. This high suction developed due to vortices (conical vortices) at the leading edges along the roof edges.

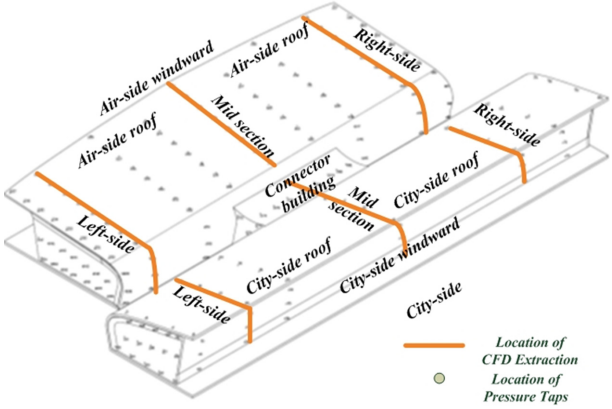


Figure 7. Represents pressure trace location on buildings.

When the wind incidence angle is 90°, the variation of lengths on the cityside and airside influences the local pressure coefficients on the windward and the roof of the city and airside. The airside separation flow influences the boundary layer of flow on the city side. Thus the stagnation pressures on the windward of the cityside are less than that of the airside. The separated flow from the windward edges of the airside causes a suction pressure at the gable end-LS for the airside and cityside; further, the pressure drops down at the verge of the connector building. Moreover, also, the airside building shear flow increases the pressure on the city side (see Figure.8 (d) and 9(d)). The contours of the local mean pressure distribution of the roof structure at 180^o for the roof surface of the airside have the suction pressure gradually decrease on the city side roof due to the flow reattachment.

3.2. Mean pressure coefficient validation with wind tunnel

This section details the distribution of local mean pressure coefficients on the complex curved-roof structure predicted by the IDDES with five different wind angle incidences using flood line contours, depicted in Figure. 8 (a-e). The pressure coefficients were obtained for various locations, namely Left Section (L.S.), Mid-section (M.S.) and Right section (R.S.), as described in Figure. 7. Figure. 9 shows the comparison of the wind tunnel and simulation pressure distribution results. It shows the distribution patterns of mean pressure on L.S., MS, and R.S. obtained from the IDDES, which agree with the wind tunnel results. The overall differences between the experimental and computational results are less than 18%; thus, the accuracy of the IDDES turbulence model is validated for predicting the mean pressure distributions on curved roof structures.

3.3. Fluctuating pressure coefficient (Cp rms)

The fluctuating nature of the atmospheric wind flow and the building's unsteady flows are the main factors for strong flow separation and reattachment that affect the roof's strength. This feature is significant for the design of a long-span roof structure.

The computationally simulated Cp_{rms} for three sections of long–span roof structure (namely: Left Section (Left), Mid-section (Mid) and Right section (Right), see Figure. 10.) are compared with the wind tunnel results. The magnitudes and patterns of rms pressure coefficients of the considered roof model mostly agree with those derived from the wind tunnel test. However, there are some differences between the results. For instance, at 40^o and 50^o AOIs behind the city-side roof, the wind tunnel showed immediate peaking of rms pressure values. In contrast, the IDDES

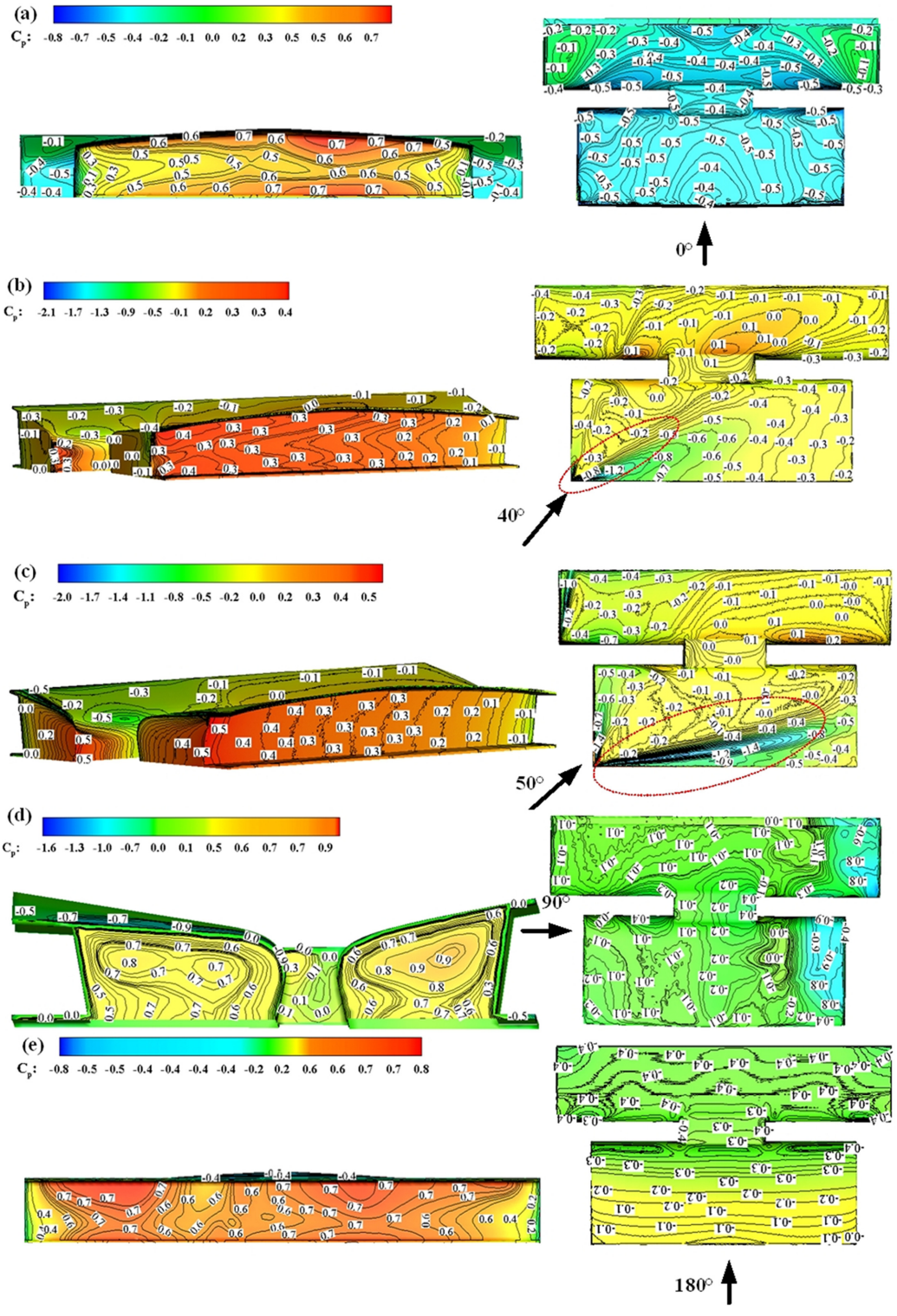


Figure 8. Contours of the mean pressure coefficient on the structure's roof location on windward and roof. (a) 0° (b) 40°(c) 50°(d) 90° and (e) 180°.

predicted peaks (of 0.45) at wake zones near the city-side roof due to the rolling up of separated vortices on the left and right sides (see also Figure. 10). The discrepancies between the computational and wind tunnel results are less than 25%. The computed rms pressure values for other locations match the measured data, and the difference is almost less than 14%.

In Figure. 10, the values of peak Cp rms at wake zones (mainly, space between city and airside roofs), apex, and dip of the roof structure exhibit high and low fluctuating

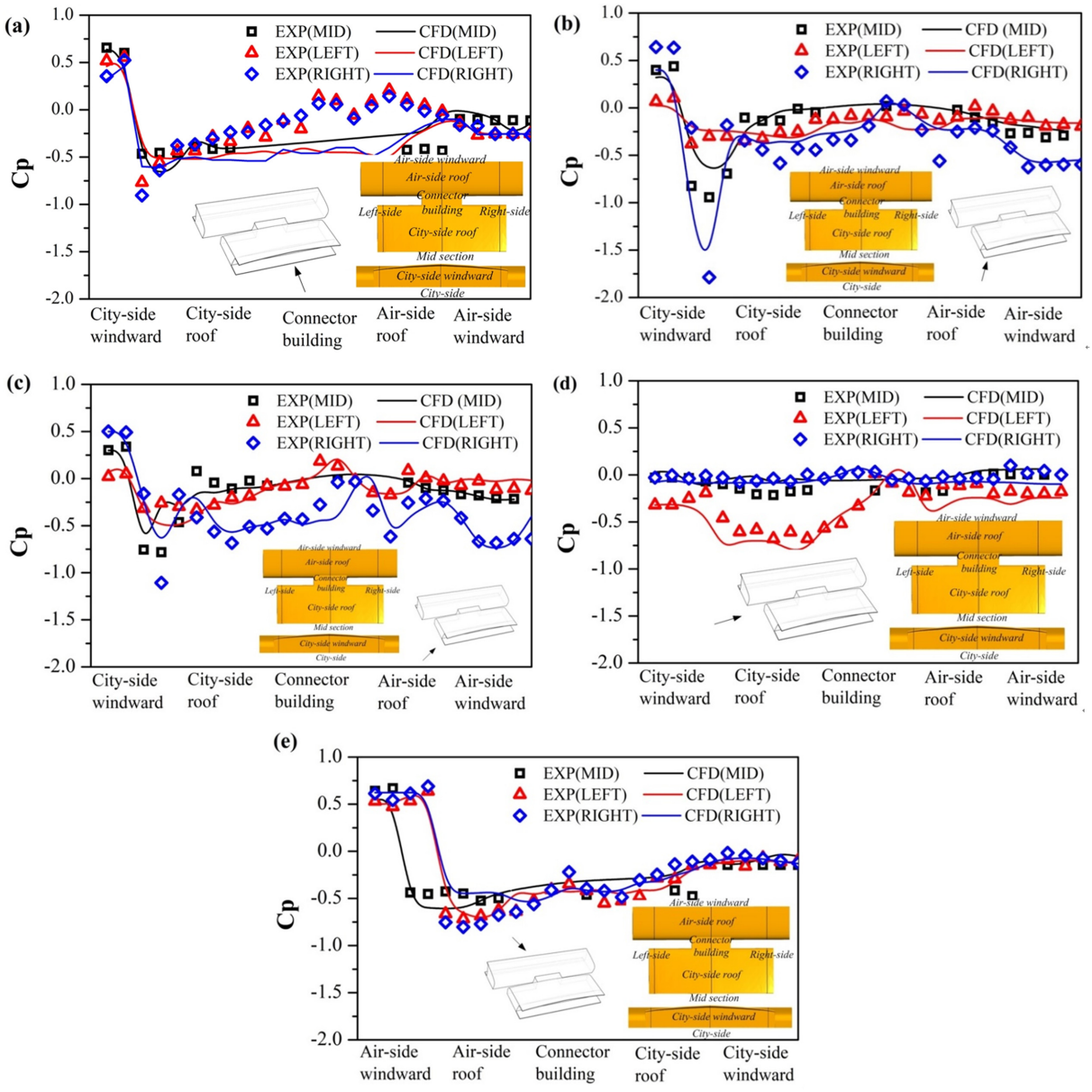


Figure 9. Comparisons of the computed local pressure coefficients for (a) 00 (b) 400 (c) 500 (d) 900 and (e) 1800.

pressures alternately. The city side windward leading edge of the roof undergoes high rms pressures at 0°, 40°, 50° and 180° AOIs. The Cp rms fluctuation was found switching between 0.045 and 0.49 between the city and air sides of the left region.

Interestingly, the areas with the high rms pressures are almost identical to those with negative mean pressures (see Figure. 9). This shows that the intermittent separation of vortices at the roof's leading edges and corners is the primary source of fluctuating pressures.

3.4. Wind flow field

Figure. 11 and 12 show the 3D wind field over the complex curved roof with the characteristics of time-averaged stream-line flow over the structure, variation of wind velocity, location of stagnation, separation, circulation, and resulting reattachments.

The flow field obtained through the computational analysis helps understand flow attributes towards the building. It helps ensure the wind-induced pressure acting on the complex structures, whereas the wind tunnel test and full-scale measurements explore the wind flow field around the building with time complexity and high expense. Besides, it has its constraints by limitations of instrumental errors and environmental conditions. However, CFD techniques, particularly the IDDES turbulence model, are very effective compared to RANS models in investigating the wind flow characteristics around the structure, resulting in more detailed wind flow field information around the building.

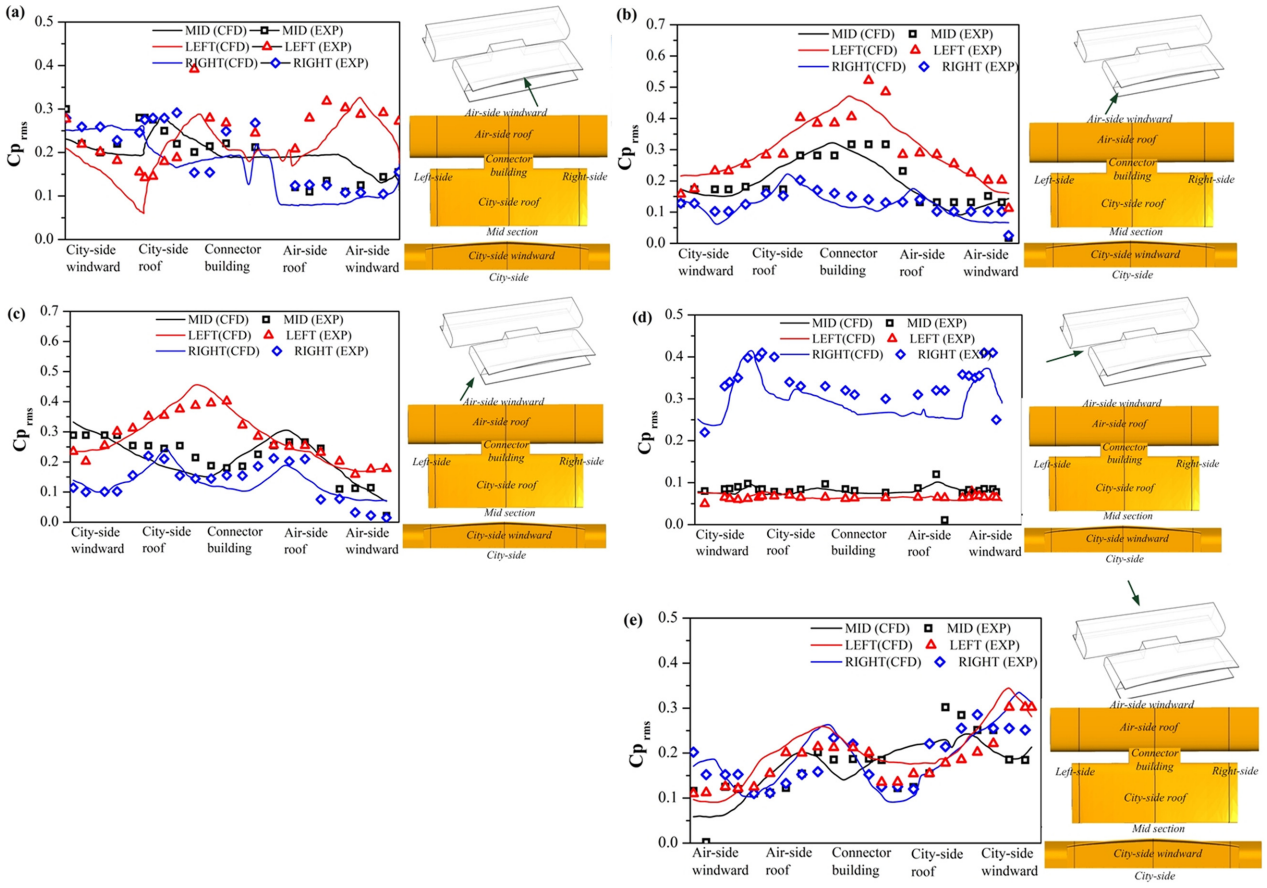


Figure 10. Fluctuating pressure coefficients (Cp rms) for the roof structure. (a) 0° (b) 400 (c) 500 (d) 900 and (e) 1800.

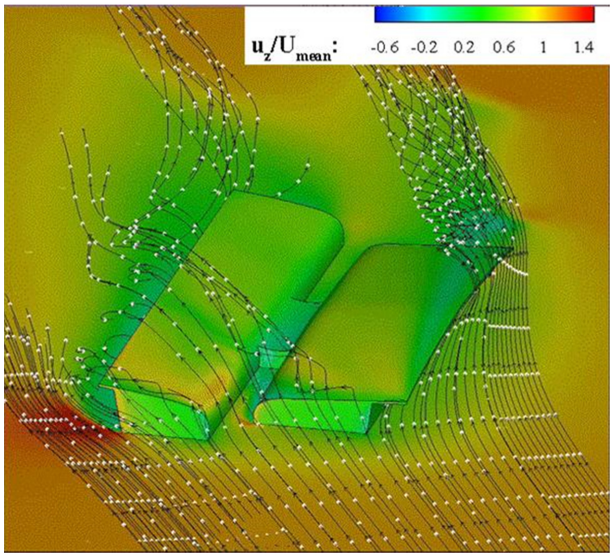


Figure 11. Instantaneous velocity contours for 40° AOI.

The instantaneous flow features for wind direction of 40° AOI, which the IDDES predicts, are presented in Figure. 11. The flow field shows that the upstream flow impinges on the roof structure; it interacts with the roof accordingly, resulting in varying velocities concerning the separation boundary layer. This interaction generates vortex-shedding modes in the boundary layer. This is one of the critical mechanisms for generating wind force on the roof structure (Dynamic pressure). Figure. 11 illustrates that the instantaneous flow patterns are much more complicated due to the strong interactions of the unsteady three-dimensional vortices, and flow around the complex long-span roof structure is complex and irregular.

The time-averaged velocity and stream-line patterns are depicted along with the horizontal (Z-Plane), and vertical plane (Y-Plane) for various critical wind incidence angles, i.e., 0°, 40°, 50°, 90°, 180° and are shown in Figure. 12(a-e).

Figure. 12(a) shows the stream-line pattern for 0° wind incidence angle in the roof structure's Y-plane. It is vivid that the velocity magnitude increases at the apex of the cityside roof due to strong shear flow, which creates the circulation above the downstream of the cityside roof. A wake region has been observed at the space between the gable ends of the city and the airside, yielding to small vortices. The wake regime is extended up to 2D downstream, and further, the flow is ripped off, leaving a small bubble that circulates and moves due to the pressure gradient.

In the case of 40°, the apex of the roof facing the wind direction leads to strong shear in the flow due to the three-dimensional slope in the curved roof leading to a small circulation just above the apex, which influences the suction in the cityside roof and is shown in Figure. 12 (b),

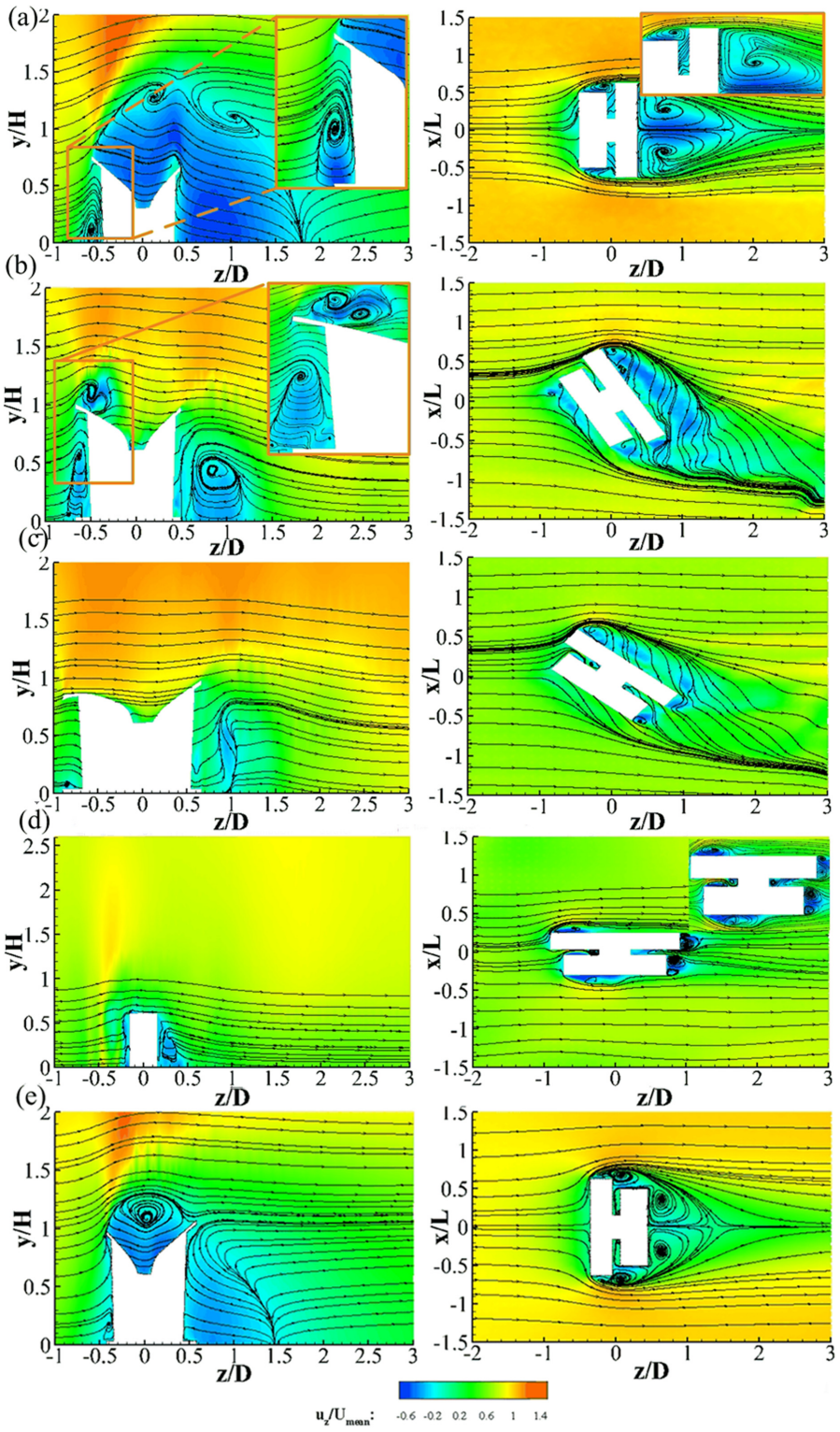


Figure 12. Mean streamlines on y = 0 and z = 0 plane. (a) 0° (b) 40° (c) 50° (d) 90° and (e) 180°.

and at the same instant, a small circulation moves over the stagnation region at the windward of the cityside. Whereas when the wind incidence angle is 50° (refer to Figure. 12 (c)), there is an absence of downwind at the windward side as seen at 40° but instead appears to have more stagnation on the structure.

When the wind incidence angle is 90° (refer to Figure. 12(d)), well-known stagnation has been observed at the windward of the cityside and airside with a strong separation along the curved edges of the city and airside. The separated

flow triggers a cavity near the edges and gets reattached towards the downstream sidewall surfaces of the cityside and airside buildings. Further, a circulation was observed at the leeward, causing a low-pressure zone and reduced velocity magnitude downstream.

At $\theta = 180°$, when the wind approaches the airside the sharp edges of the roof create a large circulation between the airside and the cityside of the building. The circulation becomes almost stagnant at the mid-section as the cityside roof's elevation is more significant than the airside and imposes a substantial suction pressure on the connector building and the adjacent roofs. The shredded vortices at the leeward end seem symmetric about the vertical axis, and the separated flow reattaches towards the downstream at a distance of 1.5 D.

The city side roof's leading edges create a large recirculation at the downward region, developing a separation and wake zone (Figure. 12 (a-e)). These wake zones are usually characterized by reattachment lengths downstream of the building. The reattachment length is a significant factor in describing the wake regions and separated flows.

4. Conclusion

The hybrid IDDES turbulence model was successfully employed to predict the airport structure's wind flow field and local pressure distribution. A detailed comparison with the wind tunnel test results was made to examine the accuracy of the employed model. From the above discussions, the following conclusions have been derived.

• The mean and rms pressure coefficient computed by the IDDES were in good agreement with wind tunnel results with the least discrepancies.

• Among the considered wind incidence angles, 0^o, 40^o, 50^o, 90^o, and 180^o seem to be more critical than other angles. The roof experienced a high negative pressure at 40^o and 50^o AOIs, whereas 0^o and 180^o AOIs exerted maximum positive pressure at the windward of the city and airside. The peak Cp rms is associated with mean peak suction pressures.

• The separation and reattachment are strongly influenced at angles 40^o and 50^o due to the corner and rolling-up vortices. The flow over the city side roof drops down gradually due to the direction and slope characteristics.

• The minimum negative pressures have been observed widely on the gable ends of the city and airside for 0^o and 180^o. Compiling the maximum and minimum pressures, it was also found that the critical angles for the roof structures are 40^o and 50^o AOI. The flow accelerates due to shear at the apex when the flow approaches the three-dimensional curved roofs and decelerates downstream, producing a strong conical vortex on the roof, resulting in fluctuating pressures and velocity.

• The pressure gradients are highly influential in complex and curve-shaped structures. It is essential to note that the CFD simulation can capture pressure gradients at every location. In contrast, the wind tunnel test can support finding pressure at discrete points of interest due to pressure tap interference.

The IDDES turbulence model can generate realistic open terrain wind simulation around the roof structure, capable of providing much information (wind flow patterns, channelling, circulation, and reattachment and velocity gradients) for wind engineering applications as the overall difference is observed to be an average maximum of 14% in comparison with experiment. It was found that the study on such a combination of the roof is limited, and it is not easy to include all kinds of roof sections in the code. Thus, this work will guide the architects and designers to know extreme pressure distribution on elevated and non-elevated curved roofs.

Nomenclature

ABL	Atmospheric Boundary Layer
AIJ	Architectural Institute of Japan
AOI	Angle of Incidence
D	Width of the building
DES	Detached Eddy Simulation
F_1& F_2	Shielding Functions
GIS	Grid Induced Separation
IDDES	Improved Delayed Detached Eddy Simulation
LES	Large Eddy Simulation
RANS	Reynolds Averaged Navier Stokes
SST	Shear Stress Transport
TKE	Turbulent Kinetic Energy
URANS	Unsteady Reynolds Averaged Navier Stokes
WMLES	Wall modeling LES
y	Maximum height in the y-direction
CP	Local pressure coefficient (mean)
$CP_{rms.}$	Fluctuating pressure coefficient
C_s	Roughness Constant (0.5)
C_μ	Empirical constant (0.09)
f_B	Blending function
f_d	Delay function
f_e	Elevating-function
l_{Hybrid}	Hybrid length scale
K_s	Sand grain roughness
U_H	Velocity at the reference height
U_x	Velocity at x-direction (m/s)
y_0	Roughness length
u^*_{ABL}	Frictional velocity of ABL
Δ	Grid spacing
ε	Dissipation of turbulence energy
κ	Karman constant
ρ	Density
ω	Specific dissipation rate

Acknowledgments

The Science and Engineering Research Board fully funded this study, Department of Science and Technology, Government of India, through the Young Scientist Scheme, 2016-2019, under YSS/2015/001395. The authors were happy to acknowledge the Wind Engineering Lab of Structural Engineering Research Center-CSIR and the Aerodynamics laboratory of VIT Chennai for their unconditional support in conducting experiments at BLWT and the computational facility.

References

ANSYS, (2020). ANSYS FLUENT user's guide. Canonsburg, PA, 15317.

Garbaruk, A., Shur, M., Strelets, M., Spalart, P. R., & Balakrishnan, R. (2010). DDES and IDDES of tandem cylinders. *Proceedings of the Benchmark Problems for Airframe Noise Computations BANC*.

Blocken, B., Stathopoulos, T., & Carmeliet, J. (2007). CFD simulation of the atmospheric boundary layer: wall function problems. Atmospheric environment, 41(2), 238-252.

Blocken, B. (2014). 50 years of computational wind engineering: past, present and future. Journal of Wind Engineering and Industrial Aerodynamics, 129, 69-102.

Lu, C. L., Li, Q. S., Huang, S. H., Chen, F. B., & Fu, X. Y. (2012). Large eddy simulation of wind effects on a long-span complex roof structure. Journal of Wind Engineering and Industrial Aerodynamics, 100(1), 1-18.

Franke, J., Hellsten, A., Schlünzen, K. H., & Carissimo, B. (2007). Best practice guideline for the CFD simulation of flows in the urban environment-a summary. In 11th Conference on Harmonization within Atmospheric Dispersion Modelling for Regulatory Purposes, Cambridge, UK, July 2007. Cambridge Environmental Research Consultants.

Franke, J., Hellsten, A., Schlunzen, K. H., & Carissimo, B. (2011). The COST 732 Best Practice Guideline for CFD simulation of flows in the urban environment: a summary. International Journal of Environment and Pollution, 44(1-4), 419-427.

Choi, J. I., Edwards, J. R., & Baurle, R. A. (2009). Compressible boundary-layer predictions at high Reynolds number using hybrid LES/RANS methods. AIAA journal, 47(9), 2179-2193.

Gritskevich, M. S., Garbaruk, A. V., Schütze, J., & Menter, F. R. (2012). Development of DDES and IDDES formulations for the k-ω shear stress transport model. Flow, turbulence and combustion, 88(3), 431-449.

Guide, R. S. D. The objectives of connection design are to transfer loads resisted by structural members and systems to other parts of the structure to form a “continuous load path";” to secure nonstructural components and equipment to the building; and• to fasten members in place during construction to resist temporary.

Guseva, E. K., Garbaruk, A. V., & Strelets, M. K. (2016, November). Application of DDES and IDDES with shear layer adapted subgrid length-scale to separated flows. In Journal of Physics: Conference Series (Vol. 769, No. 1, p. 012081). IOP Publishing.

IS 875 (Part3) - (2015). Code of Practice for Design Loads for Buildings and Structures, Third rev., New Delhi.

Ke, J. (2019). RANS and hybrid LES/RANS simulations of flow over a square cylinder. Advances in Aerodynamics, 1(1), 1-24.

Liu, J., & Niu, J. (2016). CFD simulation of the wind environment around an isolated high-rise building: An evaluation of SRANS, LES and DES models. Building and Environment, 96, 91-106.

Liu, J., & Niu, J. (2019). Delayed detached eddy simulation of pedestrian-level wind around a building array - The potential to save computing resources. Building and Environment, 152, 28-38.

Menter, F. R. (1994). Two-equation eddy-viscosity turbulence models for engineering applications. AIAA journal, 32(8), 1598-1605.

Montazeri, H., & Blocken, B. (2013). CFD simulation of wind-induced pressure coefficients on buildings with and without balconies: validation and sensitivity analysis. Building and Environment, 60, 137-149.

Ramponi, R., & Blocken, B. (2012). CFD simulation of cross-ventilation for a generic isolated building: impact of computational parameters. Building and environment, 53, 34-48.

Rajasekarababu, K. B., & Vinayagamurthy, G. (2019). Experimental and computational simulation of an open terrain wind flow around a setback building using hybrid turbulence models. Journal of Applied Fluid Mechanics, 12(1), 145-154.

Rajasekarababu, K. B., Vinayagamurthy, G., & Selvi Rajan, S. (2019, October). Experimental and computational investigation of outdoor wind flow around a setback building. In Building Simulation (Vol. 12, No. 5, pp. 891-904). Tsinghua University Press.

Rajasekarababu, K. B., & Vinayagamurthy, G. (2020). CFD validation of wind pressure distribution on a tall building under the influence of upstream terrain. Progress in Computational Fluid Dynamics, an International Journal, 20(5), 284-298.

Shur, M. L., Spalart, P. R., Strelets, M. K., & Travin, A. K. (2008). A hybrid RANS-LES approach with delayed-DES and wall-modelled LES capabilities. International journal of heat and fluid flow, 29(6), 1638-1649.

Shur, M. L., Spalart, P. R., Strelets, M. K., & Travin, A. K. (2008). A hybrid RANS-LES approach with delayed-DES and wall-modelled LES capabilities. International journal of heat and fluid flow, 29(6), 1638-1649.

Spalart, P. R. (1997). Comments on the feasibility of LES for wings, and on a hybrid RANS/LES approach. In Proceedings of first AFOSR international conference on DNS/LES. Greyden Press.

Spalart, P. R., Deck, S., Shur, M. L., Squires, K. D., Strelets, M. K., & Travin, A. (2006). A new version of detached-eddy simulation, resistant to ambiguous grid densities. Theoretical and computational fluid dynamics, 20(3), 181-195.

Strelets, M. (2001, January). Detached eddy simulation of massively separated flows. In 39th Aerospace sciences meeting and exhibit (p. 879).

Tominaga, Y., Mochida, A., Yoshie, R., Kataoka, H., Nozu, T., Yoshikawa, M., & Shirasawa, T. (2008). AIJ guidelines for practical applications of CFD to pedestrian wind environment around buildings. Journal of wind engineering and industrial aerodynamics, 96(10-11), 1749-1761.

Wang, B., Mei, G., & Xu, N. (2020). Method for generating high-quality tetrahedral meshes of geological models by utilizing CGAL. MethodsX, 7, 101061.

Xiao, L., Xiao, Z., Duan, Z., & Fu, S. (2015). Improved-delayed-detached-eddy simulation of cavity-induced transition in hypersonic boundary layer. International Journal of Heat and Fluid Flow, 51, 138-150.

Xiao, Z. X., & Luo, K. Y. (2015). Improved delayed detached-eddy simulation of massive separation around triple cylinders. Acta Mechanica Sinica, 31(6), 799-816.